Journal of Dynamics, Monitoring and Diagnostics, 2024, 3, 199-206
https://doi.org/10.37965/jdmd.2024.587

ISTP
RESEARCH ARTICLE

Strain-Insensitive Fiber Bragg Grating Composite Structure for Wide-Range Temperature Sensing

Pingyu Zhu,[1] Tingyu Huang,[1] Sheng Fan,[2] Yukun Yan,[2] Bo Peng,[2] Danli Xiong,[1] Shuai Zhang,[1] and Marcelo A. Soto[3]

[1]School of Mechanical and Electrical Engineering, Guangzhou University, Guangzhou, China
[2]Zhuzhou Times New Material Technology Co., LtD., Zhuzhou, China
[3]Department of Electronics Engineering, Universidad Técnica Federico Santa María, Valparaíso, Chile

(Received 06 July 2024; Revised 20 August 2024; Accepted 13 September 2024; Published online 14 September 2024)

Abstract: This paper reports on the design, fabrication, and temperature strain sensing performance of a fiber Bragg grating composite structure for surface mounted temperature measurements over a wide temperature range, with highly reduced strain cross-sensitivity. The fiber Bragg grating sensor is encapsulated in a polyimide tube filled with epoxy resin, forming an arc-shaped cavity. This assembly is then placed between two layers of glass fiber prepreg with a flexible pad in between and cured into shape. Experimental results, supported by finite element simulations, demonstrate an enhanced temperature sensitivity is 26.3 pm/°C over a wide temperature range of –30°C to 70°C, and high strain transfer isolation of about 99.65%.

Keywords: composite structure; fiber bragg grating; temperature sensing

I. INTRODUCTION

Wind energy, a prominent form of green and renewable energy, has seen significant progress in development globally. However, wind turbine blades (WTBs) operating in high-latitude and high-altitude regions often face extreme weather conditions, such as heavy snow and freezing temperatures, which normally reduce power generation efficiency. When WTBs are heavily covered with ice, they can be damaged or even broken [1–3]. To mitigate this issue, many modern wind turbines are now equipped with automatic de-icing systems [4,5] that heat the blades to melt the ice, ensuring safe operation. This practical solution has recently increased the demand for effective WTB icing monitoring [6,7]. Currently, five main ice detection approaches are commonly used [8,9]: ice detection, power curve monitoring, anemometer inspection [10], video monitoring [11,12], and vibration noise frequency monitoring [13]. Among these, the use of ice detection sensors is regarded as the most direct and widely used method in the field [14,15]. Although many technologies demonstrate good ice detection sensitivity based on the measurement of temperature or other parameters, they face many practical challenges [16,17]. For instance, adverse on-site climatic conditions, such as continuous heavy snow and freezing rain can impede the measurement with high accuracy. In addition, the economic cost of repetitive non-online monitoring increases significantly with the number of times the measurements need to be repeated.

Fiber Bragg grating (FBG) technology is a promising solution for monitoring WTBs due to its lightweight, fine diameter, integrated sensing transmission, and resistance to electromagnetic interference. Indeed, an ice melting system based on FBG sensing and graphene film was designed some years ago [18], providing valuable reference values for the wind turbine blade de-icing control system through wavelength drift. Unfortunately, in low-temperature environments, the thermal expansion and thermo-optic coefficients of fiber Bragg grating (FBG) materials change [19], affecting their temperature response compared to room temperature operation. This normally leads to an unwanted nonlinear response of the FBG sensor when exposed to a wide temperature range. In addition, the strain generated by the bending vibration naturally caused by the blade operation has an impact on the FBG temperature estimation [20], due to the well-known temperature-strain cross-sensitivity affecting FBG sensors [21,22]. Enhancing the linearity of thermal sensitivity and minimizing unwanted strain in FBG-based temperature sensors are essential for ensuring reliable temperature measurements in environments with mechanical vibrations and wide temperature fluctuations, such as in wind turbine blades. However, these improvements are also beneficial for a wide range of other applications that require accurate and stable temperature sensing.

This paper proposes and experimentally validates a novel FBG composite structure sensor (FBG-CSS) for surface-mounted temperature measurements over a wide range (–35°C to 70°C). The design consists of an FBG sensor encapsulated in a polyimide (PI) tube filled with epoxy resin, bent into a circular arc shape, and placed within a carbon fiber reinforced plastics (CFRP) plate with an arched three-dimensional space. This configuration enhances the FBG temperature sensitivity and its linearity, providing accurate operation in a wide temperature range. In addition, a flexible damping pad is added together with the CFRP plate, along with two layers of glass fiber reinforced glass fiber plastic (GFRP) prepreg, which are used in a sandwich configuration for hot pressing and curing. This way, this composite structure effectively minimizes strain sensitivity, ensuring reliable temperature sensing.

To further understand the operation of the FBG-CSS, finite element (FE) analysis is employed to simulate its

Corresponding author: Pingyu Zhu (e-mail: pyzhu@gzhu.edu.cn).

© The Author(s) 2024. This is an open access article published under the CC BY license (https://creativecommons.org/licenses/by/4.0/).

deformation under different temperatures. Fabricated samples are then prepared for comprehensive testing of their temperature and strain sensing performance. The obtained experimental results demonstrate that the designed FBG-CSS achieves a highly linear temperature response across a wide range, while providing a strain isolation of 99.65%. This significant strain isolation makes the proposed FBG-CSS well suited for accurate temperature measurements in WTB de-icing monitoring systems. However, we expect that the designed structure can also be used for other applications.

II. PRINCIPLE OF PROPOSED FBG COMPOSITE STRUCTURE

A. FBG SENSING PRINCIPLE

FBG sensors are produced by exploiting the photosensitive properties of fiber optic materials [22]. Using ultraviolet light, a periodic variation of the refractive index of the fiber core is created, resulting in a periodic structure. When a broadband light source is used for FBG interrogation, the wavelength that matches the grating periodicity (known as the Bragg wavelength, λ_B) is reflected, while all other wavelengths are transmitted. The reflected Bragg wavelength can be expressed as $\lambda_B = 2n_{\text{eff}}\Lambda$ [22], where n_{eff} is the effective refractive index of the fiber and the grating period Λ. As these two parameters depend on strain and temperature, temperature and strain sensing can be achieved by measuring the wavelength of the reflected light. This Bragg wavelength shift can be written as [22]:

$$\Delta\lambda_B = \lambda_B[(1 - P_e)\varepsilon + (\alpha + \zeta)\Delta T], \tag{1}$$

where λ_B represents the Bragg wavelength at a given reference temperature and zero strain, P_e describes the photoelastic coefficient, α is the thermal expansion coefficient, ζ is the thermo-optic coefficient, ε is the applied strain and ΔT is the temperature variation with respect to the reference temperature. In conventional silica single-mode fibers, the temperature sensitivity of FBG sensors is typically about 14 pm/K [22] around room temperature (i.e. 300 K), while the strain sensitivity is 1.2 pm/με [22].

It must be noted that the variations in the Bragg wavelength depend on both strain and temperature changes simultaneously. Hence, when an FBG sensor is subjected to both thermal and strain variations, it becomes impossible to distinguish between the two effects based on a single measurement of the FBG wavelength shift. This poses significant challenges for the use of FBG sensors in many applications. In addition, depending on the installation of the optical fiber, thermal expansion can induce an additional strain on the FBG. In such cases, there is an additional coupling due to temperature-induced strain, which normally enhances the overall thermal sensitivity of the FBG sensor. However, using a single FBG measurement, it becomes impossible to discriminate between changes in real strain, temperature and temperature-induced strain.

The FBG composite structure proposed in this work aims to reduce the transfer of strain originating from wind blade operation (or other applications) to the FBG sensor, thereby enabling strain-free temperature measurements. The strain energy is mainly absorbed by placing a damping and vibration-reducing material directly below the FBG sensing layer, along with the use of an arc-shaped fiber inside of a PI tube to allow the fiber to move freely and reduce the strain transferred to the FBG sensor. Additionally, the packaging utilizes a resin with a high thermal expansion coefficient at low temperatures [23] to encapsulate the FBG. This design ensures that any temperature-induced strain is effectively transferred to the embedded optical fiber, thereby improving the thermal response sensitivity and linearity of the sensing structure. Further details will be provided in the following section.

Note that the measurement and data processing procedures for the proposed FBG-CSS are identical to those used for standard FBG interrogation. This normally involves measuring the FBG reflected spectrum and performing spectral peak detection (although other procedures also exist). Therefore, no additional processing is needed for the FBG-CSS, and any commercial FBG interrogation system can be used for monitoring the packaged FBG.

B. DESIGN OF THE PROPOSED FBG COMPOSITE STRUCTURE

The proposed wide temperature range FBG-CSS is shown in Fig. 1 and consists of three main components: an outer packaging shell, an FBG-based sensing module, and a flexible pad. The outer packaging shell is made of two layers of GFRP prepreg, which encase the FBG-based sensing module and the flexible pad, all of which are cured together through hot pressing.

The sensing module is made of two layers of CFRP prepreg with a freely expandable FBG placed in the middle of an arch cavity. The upper substrate is a flat plate designed to withstand wind pressure, while the lower substrate is made with an arch groove that forms a cavity for placing the FBG sensor after hot pressed with the upper substrate. The FBG region and adjacent fiber sections are protected by a PI sleeve filled with epoxy resin, which relies on the arch cavity to bend and form an arch. The two ends of the FBG are bare fiber segments, which are fixed in straight grooves connected to the arch groove on the lower substrate and then led out. A Teflon tube is inserted at the exit of the substrate, allowing the two ends of the optical fiber to be guided out from the substrate.

The flexible pad is a silicon rubber disc with low elastic modulus that is cured at room temperature and serves as a damping layer. Located directly below the sensing module, it is used to isolate the strain caused by wind blade deformation and vibration during the operation of the wind turbine. This ensures that the wavelength change of the FBG is not sensitive to these strains.

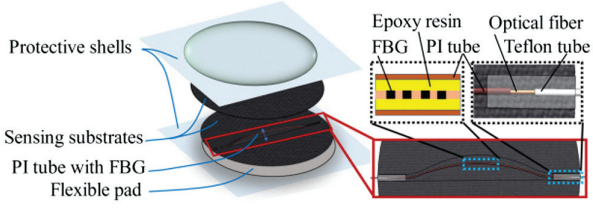

Fig. 1. Structure diagram of the proposed FBG-CSS sensing structure.

C. FBG-CSS FABRICATION

The fabrication process of the FBG-CSS is divided into several distinct steps, as shown in Fig. 2:

1. SUBSTRATE FABRICATION. Involves cutting four pieces of unidirectional CFRP prepreg, each 79 mm in diameter and 0.15 mm thick. Two of these pieces are aligned with the optical fiber direction and placed on top of the other two. The two sets of laminated CFRP are then placed into a special mold for hot pressing to create both upper and lower substrates. Then an arch-shaped cavity is created on the lower substrate, as shown Fig. 3(a).

2. SENSING MODULE FABRICATION. First, an FBG sensor is inserted into a small section of PI tube, which is filled with epoxy resin through multiple injections until fully saturated. The PI tube is slightly bent into the middle of the arch-shaped cavity on the lower substrate to allow the optical fiber and FBG sensor to expand freely and reduce strain transfer. The position of the FBG must be adjusted to ensure that it is centered within the PI tube section. The two optical fiber ends exposed outside the PI tube are fixed in straight slots on the lower substrate, and then lead them out through Teflon tubes. A thin layer of epoxy resin is applied to both upper and lower substrates and hot-pressed (see Fig. 3(b)). Note that it is important to prevent epoxy resin from seeping into the lower substrate groove to avoid adhesion to the PI tube during hot pressing.

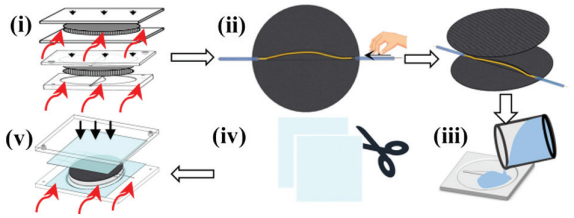

Fig. 2. Diagram of the fabrication process of the wide temperature range FBG-CSS.

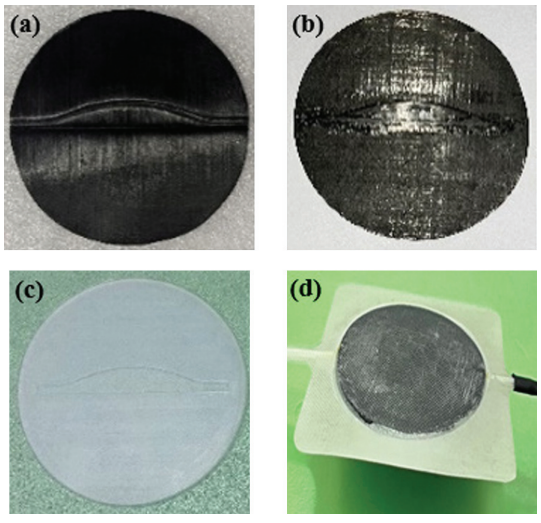

Fig. 3. Fabricated sections. (a) Lower substrate. (b) Hot-pressed sensing module. (c) Flexible pad. (d) Finished FBG-CSS sample.

3. FLEXIBLE PAD FABRICATION. For this, 6 g of silica gel are poured it into a special mold, and let it cure at room temperature for 12 hours to form a flexible pad. The mold includes a central protruding structure that matches the groove of the lower substrate, ensuring the pad has a groove at its center (see Fig. 3(c)). The bottom of the flexible pad remains flat when stacked with the lower substrate.

4. PREPARATION OF THE PROTECTIVE SHELLS. Two square pieces of glass fiber prepreg are cut with a side length of 100 mm, to be used as sandwich wraps for the entire composite structure.

5. FBG-CSS MOLDING. The convex side of the sensing module is first placed upward. Then, the flexible pads are stacked between the GFRP protective layers and placed into a dedicated mold with a cavity for hot pressing and molding (see Fig. 3(d)).

After the process, the dimensions of the fabricated FBG-CSS sensor are 100 mm in length, 100 mm in width, and 1.85 mm in height.

III. ANALYSIS AND TESTS OF FBG-CSS PERFORMANCE

A. SIMULATIONS OF TEMPERATURE-INDUCED STRAIN

To analyze the deformation of the FBG-CSS due to different temperature gradients, an FE thermal analysis is carried out in Ansys software, focusing on evaluating the thermally induced strain on the arc-shape fiber segment. Note that the parameters used in the simulation match the fabrication process and FBG-CSS samples used in the experimental validation presented in the next sections. The geometric FE model includes the lower substrate, the adhesive at both ends, and the optical fiber encapsulated by a PI tube, as shown in Fig. 4(a). Note that for the sake of simplicity the upper substrate is not considered. Given the large difference in thickness of the substrate compared to its other dimensions, the Shell181 element type is selected in Ansys for the lower substrate to provide fast computing results, at the expense of a slightly reduced simulation accuracy. The PI tube has a diameter of 0.4 mm, a wall thickness of 0.03 mm, and a length of 80 mm. Since the length of the PI tube is much larger than its diameter and wall thickness, Shell181 units are also used to model the PI tube. The optical fiber and the epoxy resin inside the PI tube are considered solid elements. The FE mesh is shown in Fig. 4(b), and the material parameters are shown in Table I.

For the analysis, the relative thermally-induce strain of the FBG-CSS is evaluated with respect to its state at a reference temperature of 25°C. The temperature of the FBG-CSS is modified between –40°C and 70°C, while the deformation of the structure and the induced strain over the optical fiber are evaluated. As examples, Figs. 4(c) and (d) illustrate the total deformation of the structure at 60°C and –35°C, respectively. When the temperature is higher than the 25°C reference, the overall structural deformation is considered positive. Results indicate that at high temperatures (e.g. 60°C as shown in Fig. 4(c)), the structure undergoes an overall expansion. On the contrary, when the temperature is below 25°C, the deformation is negative, indicating structural compression.

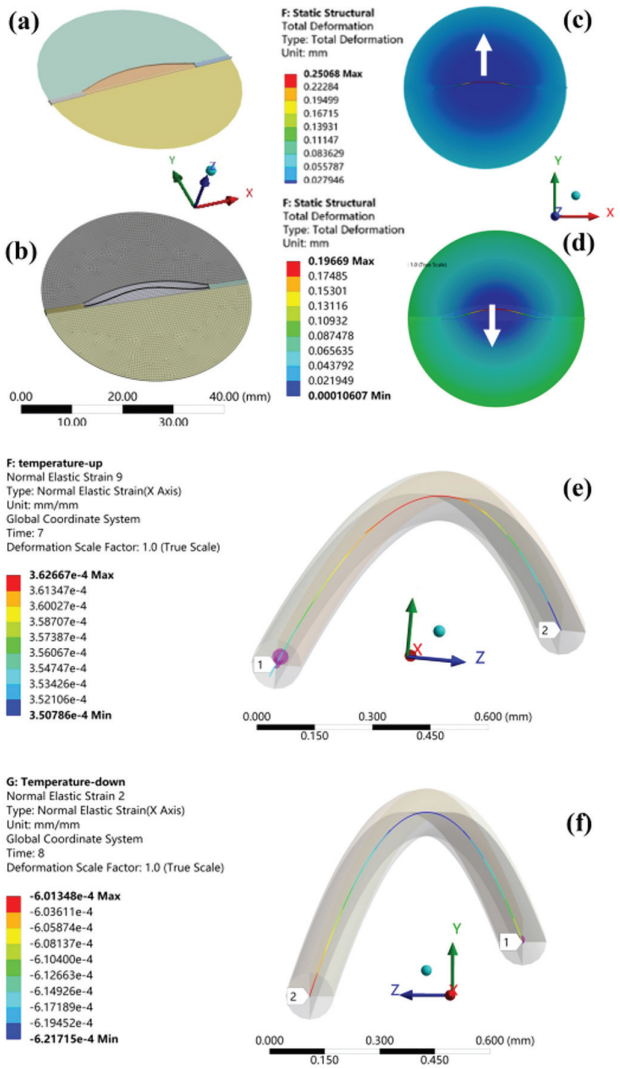

Fig. 4. FE analysis of temperature-induced strain in the FBG-CSS. (a) Geometric model used in the FE analysis. (b) Mesh of the FE model. (c) Deformation of the model when temperature increases up to 60°C. (d) Deformation of the model when temperature drops to –35°C. (e) Axial strain distribution of the FBG centerline at 60°C. (f) Axial strain distribution of FBG centerline at –35°C.

The axial strain induced at the midline position of the FBG at 60°C is shown in Fig. 4(e), indicating that the fiber is in a stretched state due to the positive strain. It can be seen that the axial strain along the entire midline is practically uniform, as evidenced by the small range of strain in colored scale of the figure. On the other hand, Fig. 4(f) shows the axial strain distribution along the midline position of the optical fiber at –35°C, which is uniform and negative, indicating that the FBG is in a compressed state.

Table I. Parameters of the materials in FE analysis

Name	Thermal expansion coefficient $\times 10^{-5}/°C^{-1}$	Elastic modulus (MPa)	Poisson's ratio
Core	0.055	77800	0.17
Coating	8.0	35	0.37
PI tube	2.0	3200	0.335
Epoxy resin	4	4898	0.403
Lower substrate	4.47	5000	0.4
Resin	3.5	2874	0.4

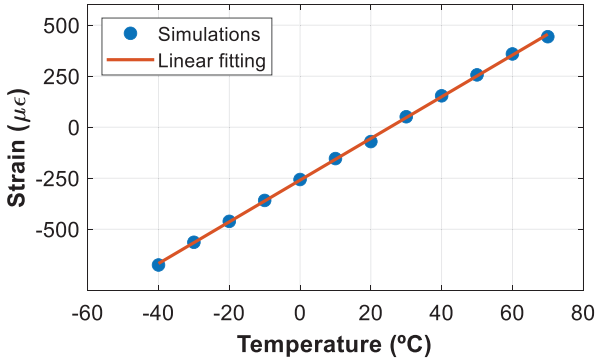

Fig. 5. Temperature-induced axial strain along the centerline of FBG region in a wide temperature range (–40°C ~ 70°C).

These simulation results are repeated at different temperatures to extract the strain induced by thermal expansion as a function of the applied temperature. Based on the strain obtained at different temperatures, the relationship between the thermally induced strain and the applied temperature is evaluated. Using the strain obtained at the midpoint of the grating region along the center line of the FBG, Fig. 5 demonstrate a linear relationship for the entire (wide) temperature range from –40°C to 70°C, with a slope of 10.25 με/°C. Considering a nominal strain sensitivity of 1.2 pm/με for the FBG sensor [21], this effect results in an additional temperature resolution of 12.3 pm/°C, thereby enhancing the overall temperature sensitivity of the FBG-CSS.

B. SIMULATIONS OF BENDING-INDUCED STRAIN

In this section the response of the proposed FBG-CSS structure to external strain is evaluated through numerical simulations using FE analysis. For this, a geometric model of the FBG-CSS attached to an equal-strength cantilever beam is established, as shown in Fig. 6(a). A displacement loading is applied to the free end of the composite cantilever beam and the strain transferred to the packaged FBG is then evaluated. The layers of the FBG-CSS are set to be bound and connected to each other, as well as to the beam, ensuring that there is no slip between the contact surfaces of each layer during overall deformation. The contact surface between the damping layer and the beam is set to be rough. Then, the entire structure, including the FBG-CSS and cantilever, is meshed using FE, as shown in Fig. 6(b).

To simulate an equivalent strain of ±3500 με on the surface of a wind turbine blade, a downward and upward displacement of 60 mm is applied to the free end of the cantilever beam in the FE software. Figs. 6(c) and (d) show the FE results of the strain distributions across the cantilever beam in the case of maximum load (both upward and downward). Results show that the strain of the cantilever beam where the FBG-CSS is located is around ±3500 με and spatially uniform. However, when the axial strain induced along the center line of the FBG grating region

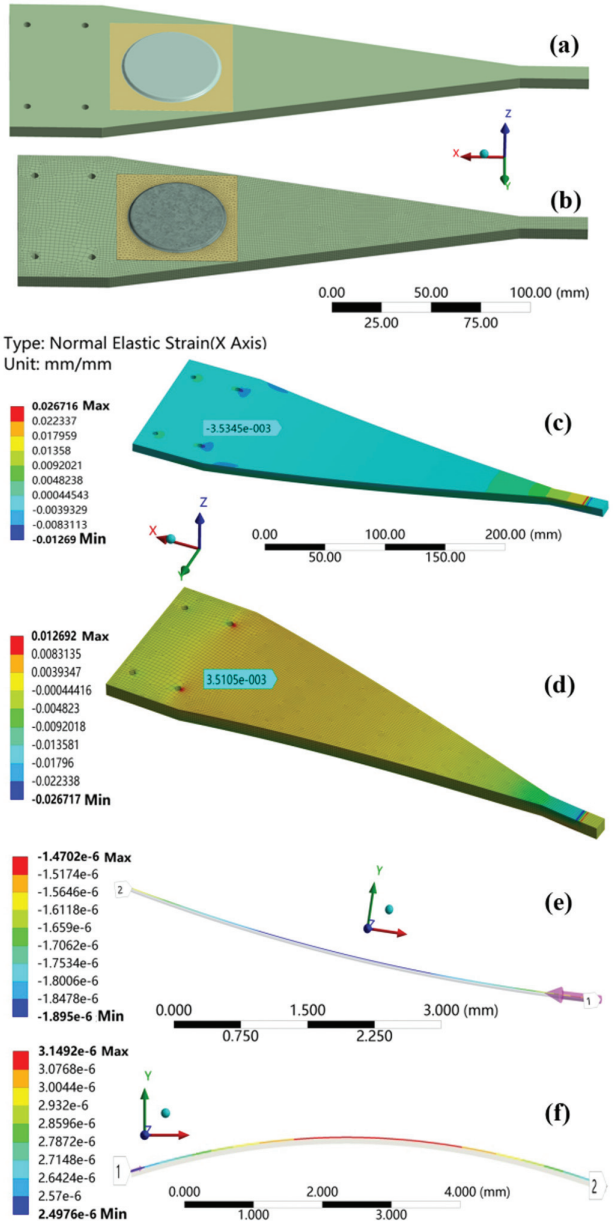

Fig. 6. FE simulation of the FBG-CSS under strain loading. (a) Geometric model of FBG-CSS glued on an equal-strength beam and (b) mesh of FE analysis. Strain distribution of the beam when applying a 60 mm displacement at the free end (c) upward and (d) downward. Strain distribution obtained along the optical fiber with a central FBG sensor under (e) upward and (f) downward displacement loadings.

is analyzed, only a strain of about –1.5 με and +3 με are found, as shown in Fig. 6(e) and Fig. 6(f), when applying the maximum negative and positive strain, respectively. These results demonstrate that the designed FBG-CSS structure has excellent strain isolation, with only about 0.09% of strain being transferred from the cantilever to the FBG.

C. TEMPERATURE RESPONSE OF THE FBG-CSS

To analyze the temperature response of the fabricated FBG-CSS structure, the experimental setup shown in Fig. 7 is used. A sample is placed in a silicon oil bath at a constant temperature, which is precisely varied in the range from –30°C to 70°C. The applied temperature and the corresponding measured FBG wavelength values are recorded with steps of 5°C. The thermal response of the FBG-CSS is shown in Fig. 8. Results demonstrate a linear relationship between the applied temperature and the center wavelength of the FBG sensor, with a slope of 26.3 pm/°C, which represents the overall temperature sensitivity achieved by the fabricated FBG-CSS. Note that this value is larger than the typical temperature sensitivity of bare FBG sensors, which is around 14 pm/°C. The additional thermal sensitivity of 12.3 pm/°C is attributed to the temperature-induced strain, matching very well the theoretical results obtained through simulations in the previous section.

The obtained temperature sensitivity coefficient is then used to evaluate the precise temperature sensing capabilities of the FBG-CSS structure. In the analysis, the sample is placd into a high-precision temperature-controlled silicone oil tank, whose temperature is varied from –30°C to 70°C. During this process, the temperature value of the FBG-CSS is recorded every 10 minutes. Figure 9 compares the temperatures obtained by the FBG-CSS (after calibration using the enhanced thermal sensitivity) with respect to the ones measured by a high-precision measurement system in the oil tank (used as a reference). Results demonstrate a very good agreement with a root-mean-square (RMS) error of 0.99°C. This indicates that both the obtained temperature

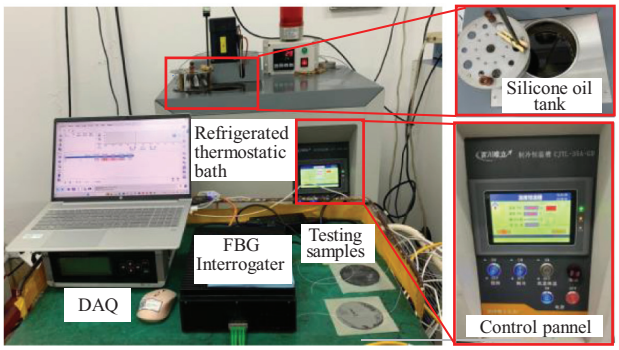

Fig. 7. Experimental setup to measure the thermal response of the FBG-CSS.

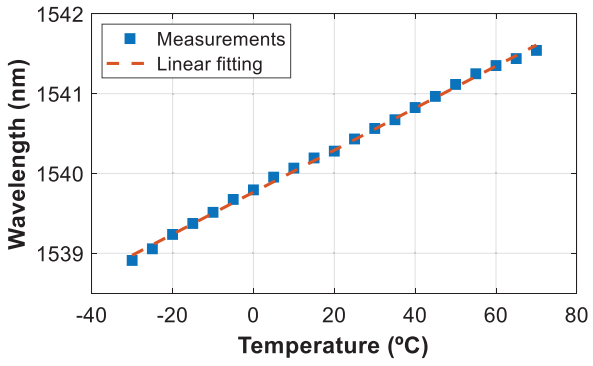

Fig. 8. Thermal response of the FBG-CSS in a wide temperature range (–30°C to 70°C).

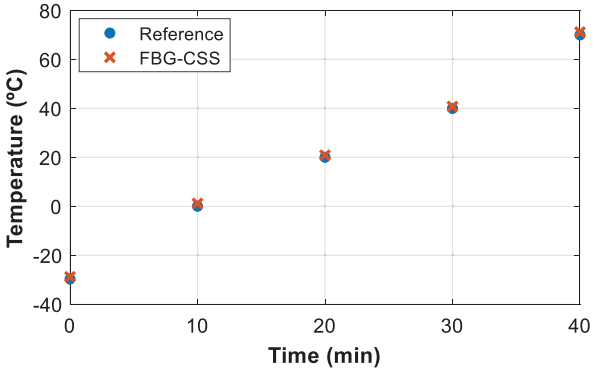

Fig. 9. Temperature measurements obtained by the FBG-CSS using the enhanced temperature sensitivity compared to the temperature of the oil tank where the sample is immersed.

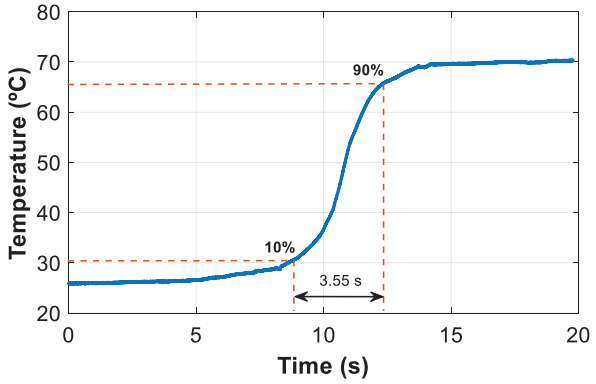

Fig. 10. Time response of the FBG-CSS temperature sensor, obtained as the 10–90% response of a step-like temperature change.

sensitivity coefficient and the calibrated temperature measurements are highly precise.

In addition, to evaluate the time response of the sensor, a temperature step is applied to the FBG-CSS. For this, the sensor, initially at room temperature (26.5°C), is immersed in hot water at 70°C, inducing a sharp step-like thermal change, as shown in Fig. 10. The time response is determined by estimating the interval between the 10% to 90% response of the temperature step, resulting in a time response of 3.55 s. Note that, although the FBG-CSS sensor is monitored every 1 ms at a 1 kHz interrogation rate, the response time is primarily governed by the thermal conductivity of the packaging materials and optical fiber.

D. STRAIN RESPONSE OF THE FBG-CSS

To evaluate the strain response of the FBG-CSS, a sample is placed on the upper surface of an equal-strength cantilever beam, along with an adjacent bare FBG sensor glued to the beam and used as a reference. The beam is first loaded with static weights of 6.5 kg, 8.5 kg, 12 kg, 16 kg, 20 kg, 25 kg, and 27 kg, which are applied to the free end of the cantilever beam. The central wavelength of the FBG-CSS and the bare FBG are recorded simultaneously. Figure 11(a) compares the strain response of the FBG-CSS with that of a reference

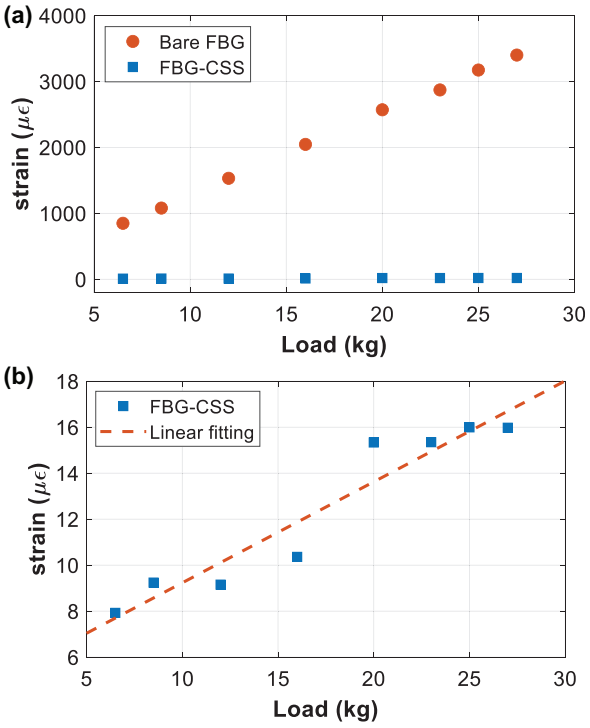

Fig. 11. (a) Strain response of the FBG-CSS compared to a reference bare FBG sensor. (b) Zoomed-in view of the highly attenuated FBG-CSS strain with a linear fitting.

bare FBG sensor, while Fig. 11(b) shows a zoomed-in view of the measurements obtained by the FBG-CSS (for better visualization). Results clearly indicate the highly attenuated strain response of the proposed FBG-CSS. For instance, under a load of 27 kg, the bare FBG sensor measures a strain of 3400 με, whereas the FBG-CSS only registers a strain of 20 με. Results in Fig. 11 demonstrate that the proposed design significantly dampens the strain transferred to the FBG sensor embedded in the FBG-CSS. Considering the strain values measured by both the bare FBG and the FBG-CSS for all the applied loads, the bare FBG sensor exhibits a load-to-strain conversion coefficient of 125.1 με/kg, while the FBG-CSS shows a coefficient of 0.44 με/kg. This indicates that the FBG-CSS measures an average strain that is only 0.35% of the strain measured by the bare FBG sensor, demonstrating a strain isolation of 99.65% provided by the proposed design. This value, although higher than the theoretically obtained from simulations, matches the same order of magnitude.

In addition, a dynamic strain evaluation is carried out by applying an oscillatory strain to the cantilever beam, while the strain at the center of the cantilever is measured by both the FBG-CSS and a reference strain gauge. Figure 12(a) shows the temporal evolution of the strain measured by both the FBG-CSS (red line) and the reference strain gauge (blue line), while Fig. 12(b) shows a zoomed-in view of the strain measured by the FBG-CSS. Results indicate that the strain values measured on the cantilever beam by the strain gauge can reach an amplitude of 3550 με, while the strain amplitude measured by the FBG-CSS is only 13.5 με. In agreement with the static strain results, this demonstrates that the designed sensor achieves excellent strain isolation.

E. IMPACT OF STRAIN ON THE MEASURED TEMPERATURE

Considering that the central wavelength measured by the FBG-CSS is still affected by a small residual strain, any strain applied to the temperature sensor will be misinterpreted as a temperature variation. Considering the temperature sensitivity of 26.3 pm/°C and a strain sensitivity reduced to 0.35% of the conventional value, each applied microstrain is expected to introduce a temperature error of approximately 0.16 mK.

This is verified using the same measurements shown in Fig. 12, where the FBG-CSS wavelength shifts induced by the applied dynamic strain are converted into temperature. Figure 13 shows the impact and error induced by residual strain on temperature measurements obtained by the proposed FBG-CSS. The figure shows temperature oscillations of about ±0.5°C around the constant room temperature of 17.4°C, resulting from the ±3546 με strain applied to the cantilever beam. Based on the 99.65% strain isolation provided by the FBG-CSS, this error is about 285 times smaller than what would be expected in a bare FBG sensor affected by strain cross-sensitivity.

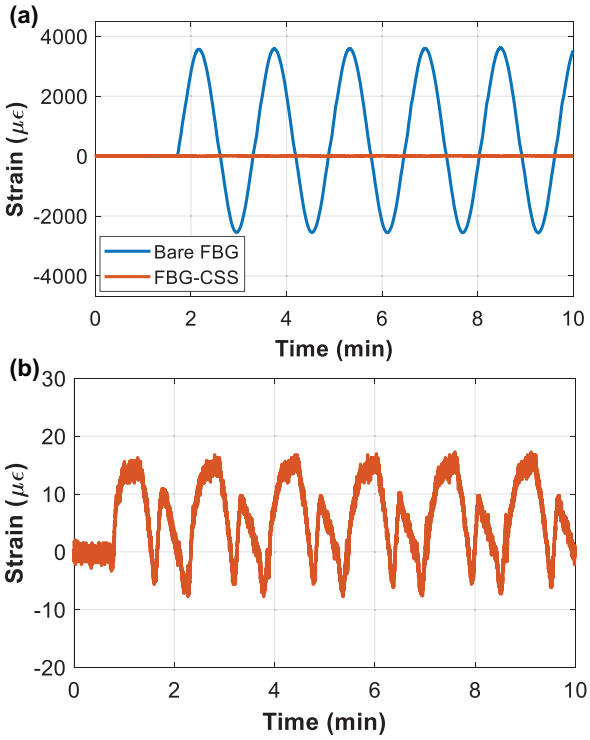

Fig. 12. (a) FBG-CSS strain response compared to a bare FBG sensor. (b) Zoomed-in view of the highly attenuated strain measured by the FBG-CSS.

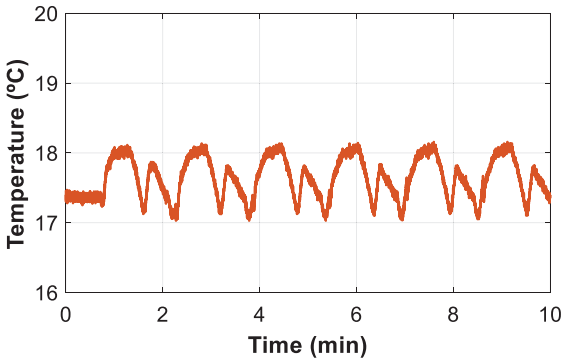

Fig. 13. Impact of strain cross-sensitivity in temperature measurements when applying an oscillatory strain of 3550 με. Measurements are obtained at a constant room temperature of 17.4°C.

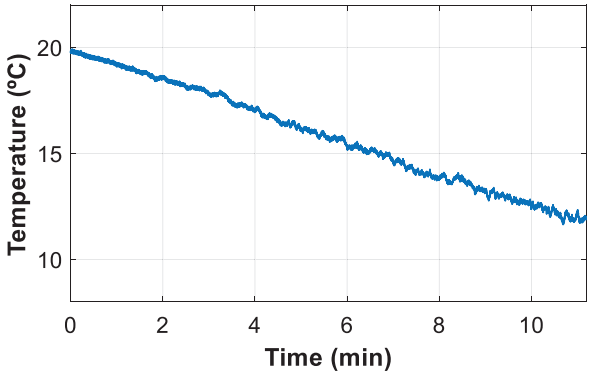

Fig. 14. Monitoring of time-varying temperatures of a cantilever beam, while being perturbed by mechanical vibrations.

Then, the fabricated FBG-CSS is applied for monitoring and diagnostics by simulating a real-world scenario, where a structure experiences time-varying temperatures while being affected by mechanical vibrations. For this experimental evaluation, a cantilever beam is placed inside a temperature chamber, whose temperature is gradually reduced from 20°C to 12°C, while the beam is perturbed by slow vibrations of 0.02 Hz and an amplitude of ±1500με. The measured temperature over time, shown in Fig. 14, exhibits minimal noise perturbations due to residual strain measured by the FBG. The RMS error of the temperature measurements remains below 0.2°C, particularly at lower temperatures where the impact of residual strain appears more pronounced.

IV. CONCLUSION

This work has proposed a new type of surface-mount FBG temperature sensor with significantly reduced strain cross-sensitivity. Based on both theoretical and experimental analyses, the following conclusions are drawn:

(1) Filling the arched cavity and PI tube with epoxy resin significantly enhances the linearity and temperature sensitivity of the embedded FBG, achieving a sensitivity of 26.3 pm/°C within the temperature range of –30°C to 70°C. This is considerably higher that than of conventional FBG sensors.

(2) The flexible pad beneath the FBG-CSS isolates 99.65% of the strain, making it ideal for reducing strain from vibrations and bending. Though originally motivated for de-icing systems in wind turbine blades, its excellent strain isolation makes it highly attractive for various other applications.

(3) The FBG-CSS can monitor the surface temperature of a vibrating structure in a variable temperature environment, like wind turbine blade flapping, providing highly accurate temperature monitoring.

ACKNOWLEDGMENTS

The authors thank the financial support from Zhuzhou Times New Material Technology Co. LtD. (Grant No. XCFDJS-2022-00004495), and Chilean National Agency for Research and Development (Basal FB0008).

CONFLICT OF INTEREST STATEMENT

The authors declare no conflicts of interest.

REFERENCES

[1] L. Y. Gao and J. R. Hong, "Wind turbine performance in natural icing environments: a field characterization," *Cold Reg. Sci. Technol.*, vol. 181, p. 103193, 2021.

[2] A. Filippatos, S. Schwab, G. Tzortzinis, and E. Madia, "In-situ identification of ice accumulation profile and vibration response at composite blades under various icing conditions," *J. Phys. Conf. Ser.*, vol. 2526, no. 1, p. 012068, 2023.

[3] Y. J. Lin and S. M. Virk, "Study of ice accretion and icing effects on aerodynamic characteristics of DU96 wind turbine blade profile," *Cold Reg. Sci. Technol.*, vol. 160, pp.119–127, 2019.

[4] O. Parent and A. Llinca, "Anti-icing and deicing techniques for wind turbines: critical review," *Cold Reg. Sci. Technol.*, vol. 65, pp. 88–96, 2011.

[5] H. Habibi et al., "A dual de-icing system for wind turbine blades combining high-power ultrasonic guided waves and low-frequency forced vibrations," *Renew. Energy*, vol. 83, pp. 859–870, 2015.

[6] J. Sabatier et al., "Ice accretion detection and anti-icing/deicing systems for wind turbine blades," In *Informatics in Control, Automation and Robotics: 14th International Conference*. Cham: Springer, July 2020, pp. 641–663.

[7] E. Madi et al., "A review of integrating ice detection and mitigation for wind turbine blades," *Renew. Sustain. Energy Rev.*, vol. 103, pp. 269–281, 2019.

[8] P. Guo and F. Infield, "Wind turbine blade icing detection with multi-model collaborative monitoring method," *Renew. Energy*, vol. 179, pp. 1098–1105, 2021.

[9] S. Shajiee et al., "Direct ice sensing and localized closed-loop heating for active de-icing of wind turbine blades," *2013 Am Control Conf.*, pp. 634–639, 2013. DOI: 10.1109/ACC.2013.6579908.

[10] P. Roberge et al., "A new atmospheric icing detector based on thermally heated cylindrical probes for wind turbine applications," *Cold Reg. Sci. Technol.*, vol. 148, pp. 131–141, 2018.

[11] K. Hacıefendioğlu et al., "Intelligent ice detection on wind turbine blades using semantic segmentation and class activation map approaches based on deep learning method," *Renew. Energy*, vol. 182, pp. 1–16, 2022.

[12] M. Kreutz et al., "Ice detection on rotor blades of wind turbines using RGB images and convolutional neural networks," *Procedia CIRP*, vol. 93, pp. 1292–1297, 2020.

[13] S. Gantasala, J. C. Luneno, and J. O. Aidanpää, "Investigating how an artificial neural network model can be used to detect added mass on a non-rotating beam using its natural frequencies: a possible application for wind turbine blade ice detection," *Energies*, vol. 10, p. 184, 2017.

[14] M. C. Homola, P. J. Nicklasson, and P. A. Sundsbø, "Ice sensors for wind turbines," *Cold Reg. Sci. Technol.*, vol. 46, no. 2, pp. 125–131, 2006.

[15] K. Wei, Y. Yang, H. Zuo, and D. Zhong, "A review on ice detection technology and ice elimination technology for wind turbine," *Wind Energy*, vol. 23, no. 3, pp. 433–457, 2020.

[16] E. Guk, C. Son, L. Rieman, and T. Kim, "Experimental study on ice intensity and type detection for wind turbine blades with multi-channel thermocouple array sensor," *Cold Reg. Sci. Technol.*, vol. 189, p. 103297, 2021.

[17] J. Simon, J. Moll, and V. Krozer, "Trend decomposition for temperature compensation in a radar-based structural health monitoring system of wind turbine blades," *Sensors*, vol. 24, no. 3, 2024.

[18] Y. B. Guo and Y. Q. Bao, "Smart Graphene Film based on FBG sensor for on-line icing monitoring and de-icing of wind turbine blade," In *The 7th World Conference on Structural Control and Monitoring(7WCSCM)*, Qingdao, China, July 2018.

[19] H. Yamada, Y. Tanaka, M. Ogata, K. Mizuno, K. Nagashima, S. Okumura, and Y. Terada, "Measurement and improvement of characteristics using optical fiber temperature sensors at cryogenic temperatures," *Phys. C*, vol. 471, pp. 1570–1575, 2011.

[20] M. Y. Liu, W. W. Zhang, and H. Song, "Study on temperature sensing characteristics of FBG in low temperature environment," *Semicond. Optoelectron*, vol. 43, no. 2, p. 327, 2022.

[21] H. Qin, P. Tang, J. Lei, H. Chen, and B. Luo, "Investigation of strain-temperature cross-sensitivity of FBG strain sensors embedded onto different substrates," *Photonic Sens.*, vol. 13, no. 1, p. 230127, 2023.

[22] A. Othonos, K. Kalli, D. Pureur, and A. Mugnier, "Fibre bragg gratings," In *Wavelength Filters in Fibre Optics*. Berlin, Heidelberg: Springer, July 2006, pp. 189–269.

[23] Z. J. Cai, H. Song, Z. Y. Zhang, and X. Y. Yao, "Cryogenic temperature characteristics of thermosetting epoxy resins coated FBG sensors," In *2021 IEEE Sensors Applications Symposium (SAS)*, IEEE, 2021, pp. 1–5. DOI: 10.1109/SAS51076.2021.9530153.